ISSN 1063-7826, Semiconductors, 2020, Vol. 54, No. 5, pp. 543–553. © Pleiades Publishing, Ltd., 2020.

SEMICONDUCTOR STRUCTURES, LOW-DIMENSIONAL SYSTEMS, AND QUANTUM PHENOMENA

Interfacial Characterization and Transport Conduction Mechanisms in Al|HfO_2|*p*-Ge Structures: Energy Band Diagram

M. A. Botzakaki[a,*], G. Skoulatakis[b], G. P. Papageorgiou[c], and C. A. Krontiras[a]

[a] *Department of Physics, University of Patras, Patras, 26504 Greece*

[b] *Department of Chemical Engineering, University of Patras, Patras, 26504 Greece*

[c] *Institute of Nanoscience and Nanotechnology, NCSR "Demokritos", Athens, 15310 Greece*

**e-mail: mpotzakaki@physics.upatras.gr*

Received December 6, 2019; revised January 15, 2020; accepted January 15, 2020

Abstract—Ge-based metal-oxide semiconductor structures exhibiting thin ALD-grown high-*k* dielectric HfO_2 films were fabricated and characterized chemically, structurally, and electrically. X-ray photoelectron (XP) spectroscopy confirms the good stoichiometry of the ALD-grown HfO_2 films. Furthermore, through the analysis of the XP spectra, the conduction and valence band offsets of HfO_2|*p*-Ge were calculated to be equal to 1.8 ± 0.2 eV and 2.8 ± 0.2 eV, respectively. $C(V)$ and $G(V)$ analysis reveals structures with a well-defined MOS behavior with D_{it} values in the range of 10^{11} eV^{-1} cm^{-2} and a dielectric constant of HfO_2 films of 20. The dominant carrier transport conduction mechanisms were studied through $J(V)$ analysis, performed at both substrate and gate electron injection. Specifically, in the low voltage region ($V < 0.2$ V), the prevailing conduction mechanism is Ohmic, with an activation energy of 0.28 eV for both substrate and gate electron injection. In the voltage range 0.4–1.5 V, the dominant conduction mechanism is Frenkel–Poole, through which the trap energy level into HfO_2 films (φ_t) is calculated to be $\varphi_t = 0.36$ eV. Schottky conduction mechanism is the prevailing one, for high applied bias voltages ($V > 3.0$ V) and high temperatures (>450 K). Applying Schottky's emission model the energy barrier heights of HfO_2|*p*-Ge and Al|HfO_2 interfaces were evaluated equal to 1.7 ± 0.2 eV and 1.3 ± 0.2 eV, respectively. Combining the XPS and $J(V)$ analysis results, the energy band diagram of Al|HfO_2|*p*-Ge structures is constructed. The calculated values of conduction and valence band offsets via XPS and $J(V)$ measurements are in very good agreement.

Keywords: ALD HfO_2, *p*-Ge, XPS, conductivity mechanisms, energy band diagram

DOI: 10.1134/S1063782620050036

1. INTRODUCTION

Germanium (Ge) is considered as an alternative to Si channel material, into future Complementary Metal-Oxide Semiconductor (CMOS) devices mainly due to its enhanced intrinsic electron and hole mobilities [1, 2]. The electron mobility of bulk Ge is almost two times higher than that of Si while the hole mobility is the highest compared even to composite III–V semiconductors such as InGa or GaAs [3]. On the other hand, the instability of dielectric Germanium Oxide (GeO_x) is a limiting factor/deterrent in implementing Ge in CMOS technology [1, 2]. Thus, the growth of a gate insulator material leading to the formation of advanced MOS devices, exhibiting simultaneously superior electrical properties and low leakage currents for higher performance and lower power consumption circuits, is critical [4–9].

The integration of high-dielectric constant gate oxides for Ge-based MOS devices has already attracted much attention due to their enhanced electrical strength and stability [9–14]. Among the basic criteria for the implementation of high-*k* oxides as gate dielectrics, two of the most crucial factors are the understanding of carrier transport mechanisms through the gate dielectric and the study of the energy band profile/diagram of the whole MOS structure (Metal | High-*k* gate dielectric | Semiconductor) through the identification of the energy barrier heights between metal | gate dielectric and gate dielectric | semiconductor, which would effectively block electrons and holes [15, 16].

Among many possible gate dielectrics, hafnium dioxide (HfO_2) seems to be one of the most promising candidates for gate dielectric [17, 18] due to, relatively to other high-*k* materials, its large band gap [19], high dielectric constant, excellent thermodynamic stability [20], and high breakdown electric field (~8.5 MV/cm) [21]. There are a lot of studies concerning thin dielectric HfO_2 films as an alternative to SiO_2 gate dielectric, in Si-based MOS structures due to the potential benefit of increasing the physical oxide thickness of the

dielectric film by taking advantage of its high permittivity value. In these studies, HfO_2 films were extensively characterized through capacity-voltage measurements [22, 23], $J(V)$ measurements leading to the identification of conductivity mechanisms through the film [18, 22, 24, 25], XPS analysis [26], TEM analysis [27] and AFM analysis [23], etc. Although, there are studies concerning HfO_2 as a possible gate dielectric onto *p*-Ge semiconducting substrates, these studies are mainly focused on the optimization of the electrical response of the structures through the passivation of the interface $HfO_2|p$-Ge via the insertion of interlayers (IL) between $HfO_2|IL|p$-Ge [1, 12, 28–34] or other methods [35–38]. The evaluation of the energy barrier heights of Metal$|HfO_2$ and $HfO_2|p$-Ge leading to the construction of energy band diagram from experimental results, as well as the systematic study of the conduction mechanisms of the structures, have not been addressed in detail.

In the present work, thin HfO_2 dielectric films were directly deposited via atomic layer deposition (ALD) technique onto *p*-Ge semiconducting substrates. A systematic study of the conductivity mechanisms of the structures was performed, in structures with 10 and 15 nm thickness of HfO_2, for a wide temperature and voltage range. Furthermore, the chemical and electrical characterizations on $HfO_2|p$-Ge and Al$|HfO_2$ interfaces were performed via X-ray photoelectron spectroscopy analysis (XPS) and electrical measurements, respectively, leading to the construction of the energy band profile of the whole structure Al$|HfO_2|p$-Ge, combining the experimental results of these two independent techniques.

2. EXPERIMENTAL

Thin dielectric HfO_2 films with thicknesses varying from 3 to 15 nm were grown onto Czochralski grown p-type (100) semiconducting Ge substrates with 0.04–0.4 Ω cm resistivity, supplied from Umicore Inc. Prior to the deposition procedure, Ge substrates were chemically cleaned, in order to remove the organic residues and the native oxide from the substrates, through five alternating immersions into an (i) HF solution 2% v/v and (ii) deionised water (18.2 MΩ) for 15 and 20 s, respectively [28].

A Savannah-100 ALD (Cambridge-Nanotech, USA) system was used, with tetrakis(dimethylamido)hafnium [$Hf(NMe_2)_4$] [39, 40] (heated at 75°C) as deposition precursor and H_2O and co-reactant/oxidant. ALD films were grown through the repetition of identical deposition cycles, each of which includes the precursor and oxidant pulses for 0.15 and 0.015 s, respectively. Each pulse was followed by a 5-s time interval of the carrier gas (N_2), purging at a flow rate of 20 sccm. The duration between pulses (5 s) as well as the growth per cycle (GPC) of the film (GPC = 0.94 Å/cycle) was defined by the temperature of the deposition, which was kept constant at 250°C. Thus, according to ALD specifications, for the growth of 5, 10, and 15 nm of HfO_2 films at 250°C, the repetition of 54, 106, and 160 cycles was required. HfO_2 monolayers were grown through a double-exchange chemical reaction, taking place in the chamber of the deposition system, of the form (1) [41]

$$Hf[N(CH_3)_2]_4 + 2H_2O \rightarrow HfO_2 + 4HN(CH_3)_2. \quad (1)$$

The chemical composition and thickness of all the ex situ prepared samples were investigated using XPS. The experiments were performed in an ultra-high vacuum (UHV) chamber. For the XPS measurements, a non-monochromatized AlK_α X-ray source (1486.6 eV) was used. Photoemission spectra were collected via a Leybold EA-11 hemispherical energy analyzer operating at constant pass energy of 100 eV at 0-degree take-off angle. To compensate for the electrostatic charging, the predominant aliphatic contribution to the C1s peak at 284.8 eV binding energy was used as a reference in all the X-ray photoelectron spectra. XPS spectra were analyzed using the XPS peak4.1 software. A Shirley-type background correction was used inside the region of analysis with three average points at end points.

The structural characterization of the samples was carried out through transmission electron microscopy (TEM), using a Philips CM20 TEM, operating at 200 kV. The cross-sectional specimens were prepared through a mechanical thinning and an ion beam milling.

For the electrical characterization of the grown films, patterned Al$|HfO_2|p$-Ge capacitive structures were performed via magnetron sputtering using photolithography and lift-off processes. The thicknesses of the Al gate top electrodes were varying between 200–300 nm. InGa eutectic alloy and silver conductive paste were used as the back ohmic contact of the structures. Capacity–voltage $C(V)$ measurements were performed via an ALPHA-N broadband dielectric spectrometer (Novocontrol). Current–voltage measurements were performed through a Keithley 2611A sourcemeter both for substrate and gate electron injection in the temperature range between 163 and 533 K and gate voltage range from +5.0 to –5.0 V.

3. RESULTS AND DISCUSSION

In Fig. 1, the Hf4f core-level doublet spectrum with a spin-orbit splitting of 1.7 eV and an area ratio 3:4 is presented. The $Hf4f_{7/2}$ and $Hf4f_{5/2}$ components appear at binding energies 16.8 ± 0.1 eV and 18.5 ± 0.1 eV, respectively, for the thick (15 nm) HfO_2 film that was used as a reference. The binding energies of Hf4f core-level doublet spectra for 3-, 5-, and 8-nm ultra-thin films of HfO_2, grown on *p*-Ge wafers are shifted by 0.2 eV towards higher binding energies with-

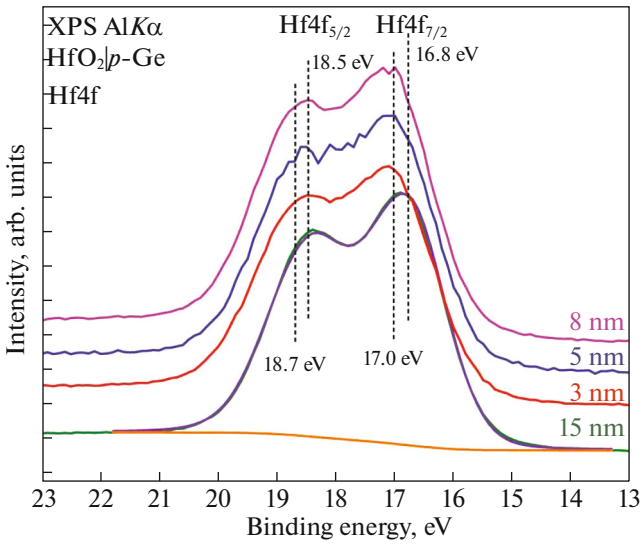

Fig. 1. The Hf4f XPS peaks of the Ge|HfO_2 structure.

out any change in the spin-orbit splitting, area ratio or shape of the peaks and are in agreement with the reported binding energies for HfO_2 [42].

Since there is an overlap of the Ge3d and the Hf5p peak, in order to investigate the substrate contribution, the Ge3p XPS peak (Fig. 2) was measured instead of the strongest Ge3d peak. The Ge3p XPS peak appears as a double peak, $Ge3p_{1/2}$ and $Ge3p_{3/2}$, due to the spin-orbit interaction in all structures. As it is shown at the normalized spectra in Fig. 2, the Ge3p peak was fitted by a doublet with 4.1 eV splitting and an intensity ratio of 2:1 with the $Ge3p_{1/2}$ and $Ge3p_{3/2}$ peaks at the binding energies of 125.7 ± 0.1 eV and 121.6 ± 0.1 eV, respectively, corresponding to elemental Ge^0 [43]. It must be pointed out that no Ge sub oxides were detected between *p*-Ge and the HfO_2 film.

For the calculation of the HfO_2 thin film thickness, the method reported by Ladas et al. [44] was used. The thickness was calculated from simulations of measured intensity ratios Ge3p|Hf4f, using appropriate databases for the relative sensitivity factors (RSF) for the used analyzer of the Ge3p and Hf4f photoelectrons and the respective escape depths in different layers. The values of the HfO_2 film calculated by XPS analysis are shown in Table 1 and the estimated uncertainty is ±10%.

In Fig. 3, the valence band maximum of the (a) Ge|15-nm HfO_2 and (b) Ge wafer were determined to be 2.6 ± 0.1 and 0.0 ± 0.1 eV, respectively.

The valence band offset (ΔE_V) and the conduction band offset (ΔE_C) at the Ge|HfO_2 interface were determined according to Kraut's methodology [45] by the following equations:

$$\Delta E_V = (E_{CL}^{Ge3p_{3/2}} - E_{VBM}^{Ge})^{Ge\ wafer} - (E_{CL}^{Hf4f_{7/2}} - E_{VBM}^{HfO_2})^{15\,nm\,HfO_2} - (E_{CL}^{Ge3p_{3/2}} - E_{CL}^{Hf4f_{7/2}})^{Ge/HfO_2}, \quad (2)$$

$$\Delta E_C = E_g^{HfO_2} - E_g^{Ge} - \Delta E_V, \quad (3)$$

where the energy differences $(E_{CL}^{Ge3p_{3/2}} - E_{VBM}^{Ge})^{Ge\ wafer} - (E_{CL}^{Hf4f_{7/2}} - E_{VBM}^{HfO_2})^{15\,nm\,HfO_2}$ between the selected core levels and the valence band are determined for bulk Ge and for a thick HfO_2 film. The term $(E_{CL}^{Ge3p_{3/2}} - E_{CL}^{Hf4f_{7/2}})^{Ge/HfO_2}$ is defined as the energy difference between the core levels in the thin (3-, 5-, and 8-nm) HfO_2 films on Ge.

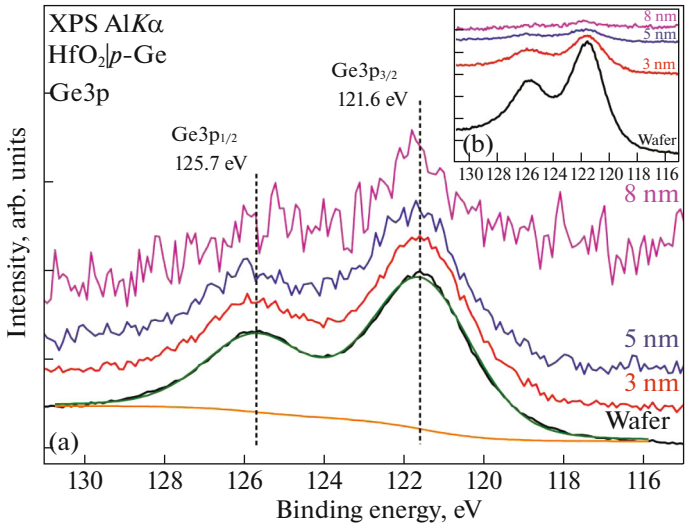

Fig. 2. The Ge3p XPS peak of the Ge|HfO_2 structure: (a) normalized and (b) as-received spectra.

Table 1. Calculated HfO_2 thickness

Calculated thickness, nm	3.2	4.9	8.5
Nominal ALD thickness, nm	3	5	8

Inserting the values of XPS analysis in Eq. (2), the valence band offset value of $\Delta E_V = 2.8 \pm 0.2$ eV was extracted. Finally, the conduction band offset value ($\Delta E_C = 1.8 \pm 0.2$ eV) was determined using Eq. (3) where $E_g^{HfO_2}$ and E_g^{Ge} are the band gaps of HfO_2 [19, 46] and Ge [47], respectively.

Figure 4 shows a cross-sectional high-resolution (HR) TEM micro image of the 5-nm $HfO_2|p$-Ge deposited at 250°C. At first, HfO_2 thin film appears to be a uniform and dense thin layer with a relatively sharp Ge|HfO_2 interface. The analysis of the TEM micro image reveals that the thickness of the ALD-grown HfO_2 was around 4.5–4.8 nm, in very good agreement with the expected one from ALD (nominal thickness 5 nm).

In the interface between $HfO_2|p$-Ge, an ultrathin amorphous interlayer of about 0.5 nm is present, attributed to GeO_x monolayers [48–51].

Figure 5 depicts the capacitance-voltage characteristics as a function of frequency at room temperature for Al|10-nm $HfO_2|p$-Ge structure deposited at 250°C. Typical $C(V)$ behavior is observed, with the three distinct regions of accumulation, depletion, and inversion.

Note here that in the depletion/weak inversion regime, the appearance of the so called "humps" is a common feature in Ge-based $C(V)$ curves, and is attributed to minority carrier response of Ge [52]. Accumulation at MOS structures with p-type semiconductors occurs for negative voltages where the negative charge on the gate attracts holes, which are the only positive charges available in the semiconductor, from the substrate to the oxide-semiconductor interface. The holes concentration at the interface is above the bulk value, thus leading to the so-called accumulation state. Depletion occurs for low positive voltages. The positive voltage on the gate depletes the majority carriers, i.e., holes in the semiconductor's surface. Inversion occurs at high positive voltages. In addition to the depletion layer charge, a negatively charged inversion layer forms at the oxide-semiconductor interface (minority carriers, i.e., electrons), thus the semiconductor surface inverts its conduction type from p-type to n-type [53]. Furthermore, due to the fact that, compared to Si, Ge exhibits a lower, almost half of that of Si, energy band gap E_g ($E_g = 0.67$ eV) as well as a much larger intrinsic carrier concentration (n_i), the "low frequency $C(V)$ behavior" is observed at, relatively to Si, higher frequencies [2].

The dielectric constant of HfO_2, calculated from the analysis of the $C(V)$ curves and XPS results (thickness evaluation) is found to be equal to 20, typical value according to the literature [37, 54].

Inset of Fig. 5 depicts the $C(V)$ and $G(V)$ curves for the frequency of 900 kHz. The conductance (G) peak, located in the depletion/weak inversion regime, suggests that the loss mechanism is attributed to density of interfacial traps D_{it} [55]. The evaluation of D_{it} was performed through Hill–Coleman method [56], which is mathematically expressed by Eq. (4)

$$D_{it} = \frac{2}{qA}\frac{G_{m,\max}/\omega}{(G_{m,\max}/C_{ox}\omega)^2 + \left(1 - \frac{C_m}{C_{ox}}\right)^2}, \quad (4)$$

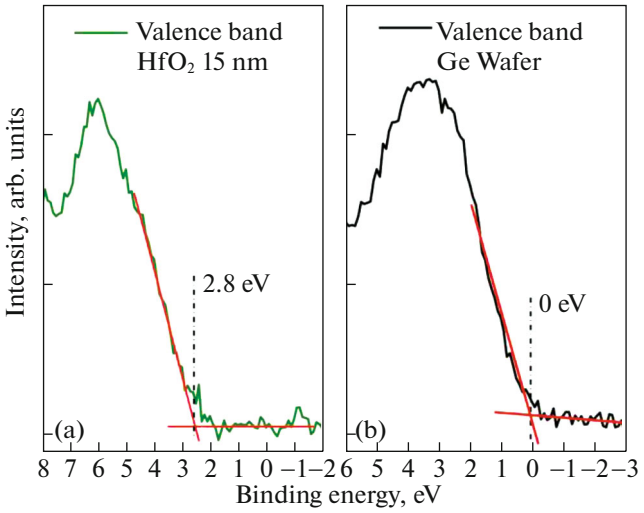

Fig. 3. The valence band XP spectra of (a) Ge|15-nm HfO_2 and (b) Ge wafer.

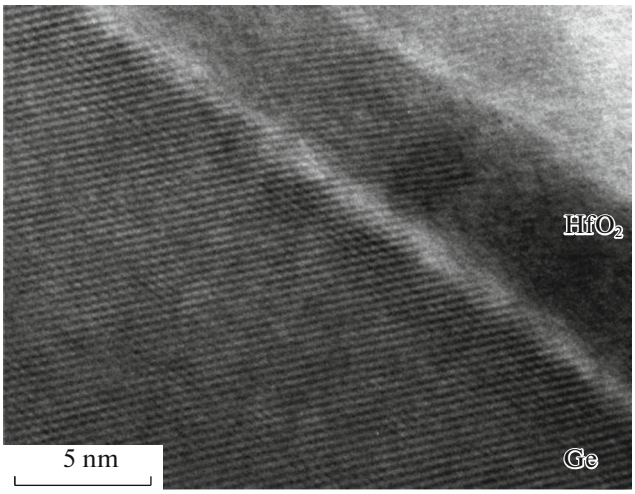

Fig. 4. HR TEM micro image of a 5-nm $HfO_2|p$-Ge structure.

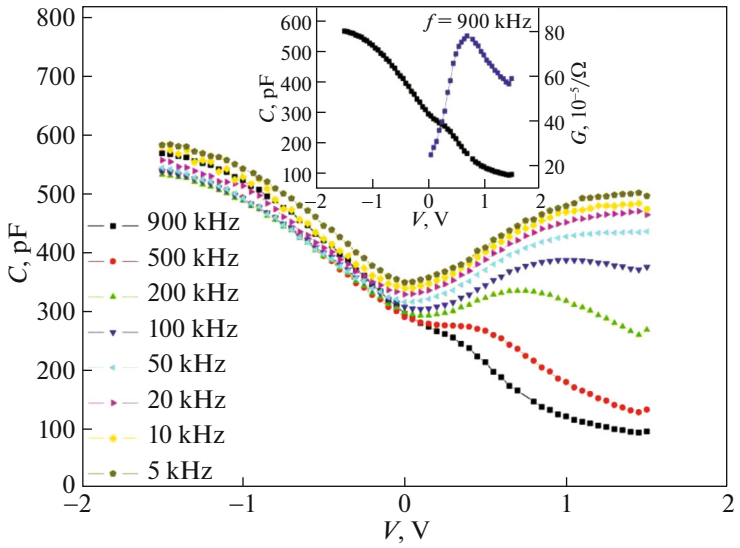

Fig. 5. $C(V)$ characteristics as a function of frequency for Al|10-nm HfO_2|p-Ge structures Inset: $C(V)$ and $G(V)$ curves at 900 kHz for Al|10-nm HfO_2|p-Ge structures.

where q is the electron charge, A is the gate area, ω is the radial frequency, $G_{m,\max}$ is the maximum measured conductance, C_{ox} is the maximum capacitance located in the accumulation regime, and C_m is the measured capacitance at the peak of the conductance. The calculated D_{it} values equal to 7×10^{11} eV^{-1} cm^{-2}.

The same analysis (not shown here) was performed for Al|5-nm HfO_2|p-Ge structures, deposited at 250°C. Values of equivalent oxide thicknesses, permittivity values as well as density of interfacial traps for both tested structures are summarized in Table 2.

It is well known that when an electric field is applied to a MOS structure, the leakage currents are attributed to various conduction mechanisms, each one exhibiting different electric field and/or temperature dependence [56]. Thus, the study of the conduction mechanisms, as well as the evaluation of the energy barrier heights of Al|HfO_2 and HfO_2|p-Ge, demand the analysis of $J(V)$ measurements as a function of both temperature and applied bias voltage.

In order to identify the carrier transport mechanisms through the structures, a second batch of samples, of 15 nm of HfO_2 films, were prepared, following the exactly same conditions, in order to reassure that the grown films are thick enough to prevent tunneling currents (bulk HfO_2 film). Figure 6 depicts the $J(V)$ measurements of Al|15-nm HfO_2|p-Ge structures in the temperature range between 163 to 393 K and applied bias voltages from −1.5 to 1.5 V under both substrate and gate electron injection. Note here that positive applied voltages refer to plus (+) on the gate Al electrode while negative applied voltages refer to minus (−) on the gate Al electrode.

Although $J(V)$ characteristics appear almost symmetrical for substrate (positive applied voltages) and gate (negative applied voltages) electron injection, it is clear that the leakage currents in the case of substrate electron injection are affected more by the temperature. This is better understood if someone notice that, in the measured temperature range, leakage currents at +1.5 V increase by almost 2 orders of magnitude while at −1.5 V by almost 1 order of magnitude.

In order to determine/identify the mechanism(s) governing the observed behavior for both substrate and gate electron injection, several conduction mechanisms were tested in each voltage and temperature region.

Figures 7a and 7b presents the $\ln J$ vs. $\ln E$ diagram in the low positive and low negative applied bias voltage region ($V < 0.2$ V) and temperatures from 253 to 393 K, respectively.

Table 2. Dielectric constant, density of interfacial traps and EOT values for Al|10-nm HfO_2|p-Ge and Al|5-nm HfO_2|p-Ge structures

Structure	D_{it}, 10^{12} eV^{-1} cm^{-2}	Dielectric constant k	EOT, nm
Al|10-nm HfO_2|p-Ge	0.7	20	2.0
Al|5-nm HfO_2|p-Ge	2.0	16	1.3

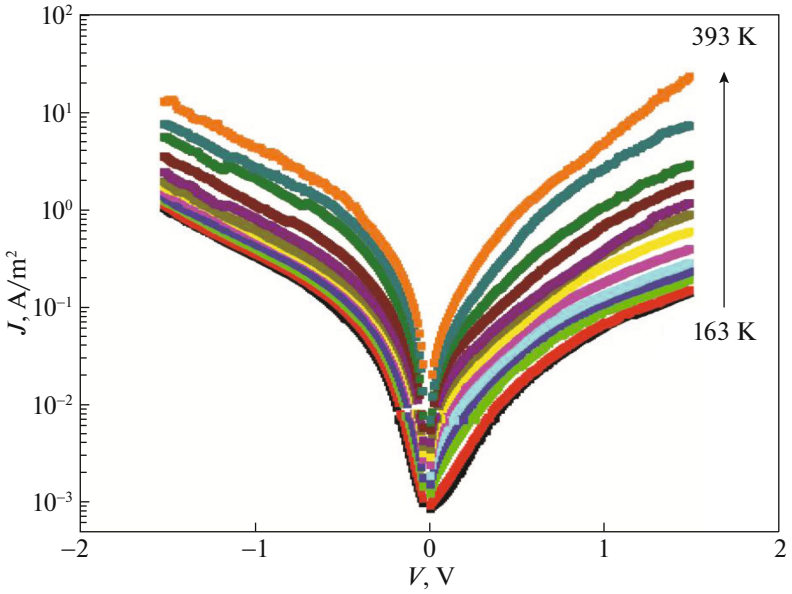

Fig. 6. $J(V)$ characteristics of Al|15-nm HfO_2|p-Si capacitor structures, under substrate and gate electron injection, in the temperature range from 163 to 393 K.

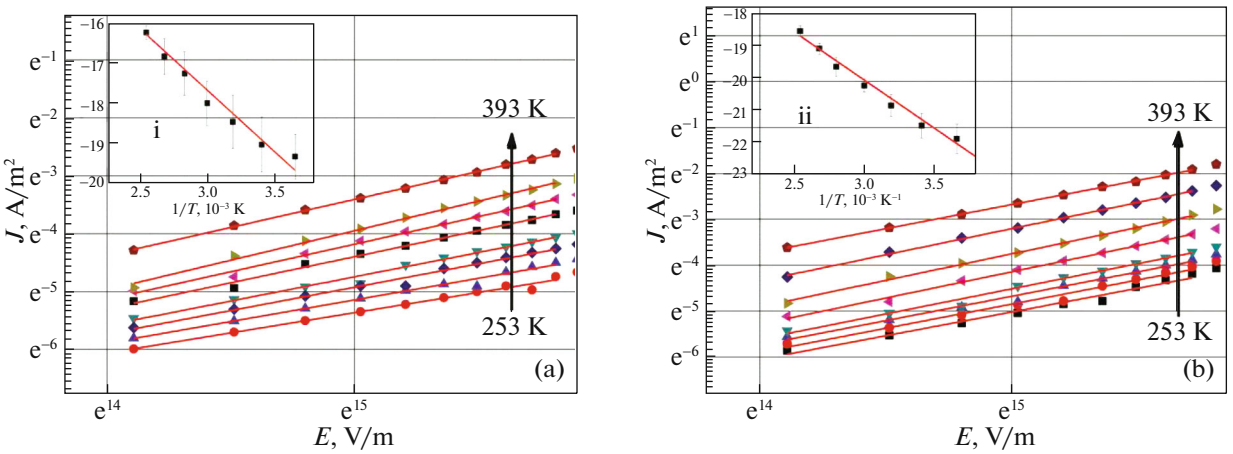

Fig. 7. $J(E)$ (both in logarithmic scale) characteristics for applied gate voltages lower than 0.2 V and temperatures between 253 and 393 K for (a) substrate electron injection and (b) gate electron injection. Insets: Arrhenius plot for low (i) positive and (ii) negative voltages in the same temperature range.

It is obvious that in the voltage and temperature region, the current exhibits a linear voltage dependence in the $J(E)$ logarithmic-scale diagram (solid lines) with a calculated slope of about ~1.0. This is a strong indication that the prevailing conduction mechanism is Ohmic described by Eq. (5):

$$J = qN_c\mu Ee^{\frac{-E_{act}}{kT}}, \quad (5)$$

where J is the current density, q is the electron charge, μ is the electron mobility in insulator, N_c is the effective density of states in the conduction band, K is Boltzmann constant, T is the absolute temperature, and E_{act} is the electron activation energy [57].

In order to evaluate the Ohmic's conduction activation energy (E_{act}), Arrhenius plots, as shown in the insets of Figs. 7a and 7b, were performed, for positive and negative applied bias voltages respectively. The activation energy of the Ohmic conduction mechanism is calculated, in both cases equal to 0.28 eV.

In order to identify the dominant conduction mechanism, in the case of substrate electron injection and for voltages higher than 0.5 V, $\ln(J/E)$ as a func-

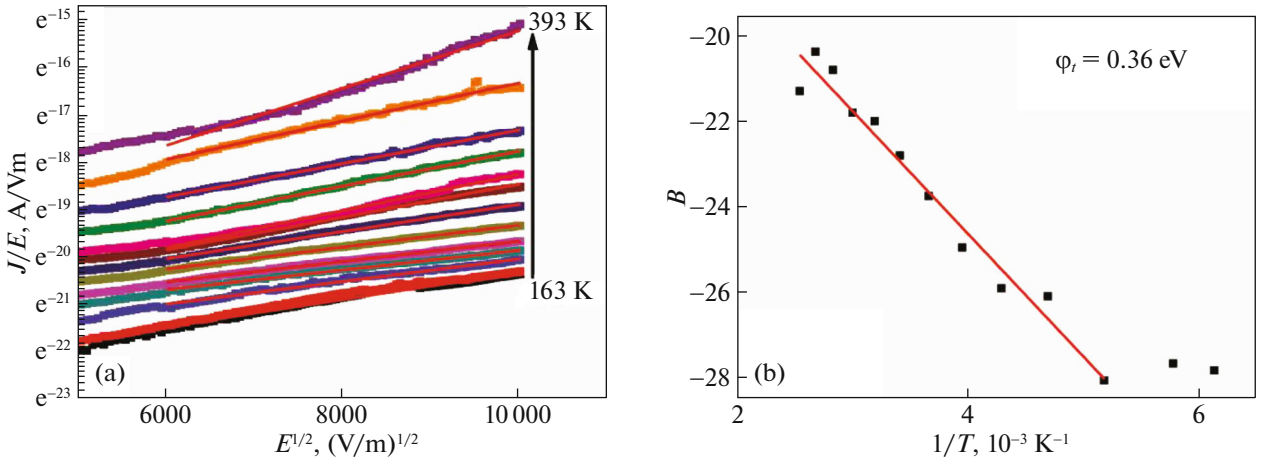

Fig. 8. (a) $\ln J/E$ vs. $E^{1/2}$ characteristics for substrate electron injection at applied voltages higher than 0.38 V in the whole temperature range. (b) Intercept B as a function of $1/T$ in the same temperature range.

tion of $E^{1/2}$ diagram was constructed (Fig. 8a), with temperature as a parameter.

It is clear that for values of $E^{1/2}$ higher than 5×10^3 $(\text{V/m})^{1/2}$ (i.e. $V > 0.38$ V), a linear dependence of $\ln(J/E)$ vs. $E^{1/2}$ is present (solid lines). Therefore, the prevailing conduction mechanism is Frenkel–Poole (FN), which is mathematically expressed through Eq. (6) [58]:

$$J = (qN_c\mu)Ee^{\frac{-q(\varphi_t-\sqrt{qE/\pi\varepsilon\varepsilon_0})}{kT}}, \quad (6)$$

where J is the current density, q is the electronic charge, N_c is the density of states in the conduction band, μ is the mobility, E is the electric field, φ_t is the trap energy level in HfO_2 thin films, T is the absolute temperature, k is the Boltzmann's constant, ε_0 is the permittivity of free space, and ε is the dynamic electric constant of HfO_2.

The analysis of FP equation

$$\ln\frac{J}{E} = \ln(qN_c\mu) - \frac{q\varphi_t}{kT} + \frac{\sqrt{q^3/\pi\varepsilon\varepsilon_0}}{kT}\sqrt{E}, \quad (7)$$

reveals that the slope of the solid lines (Fig. 8a), at each temperature, corresponds to $\frac{\sqrt{q^3/\pi\varepsilon\varepsilon_0}}{kT}$ value, while their intercepts (B) to $\ln(qN_c\mu) - q\varphi_t/kT$. Thus, through the slope of the dependence of B as a function of the inverse temperature ($1/T$), shown in Fig. 8b, the evaluation of the trap energy level into HfO_2 films (φ_t) is possible. A value of $\varphi_t = 0.36$ eV is calculated.

According to the previous analysis, Fig. 9a depicts the dependence $\ln(J/E)$ as a function of $E^{1/2}$ with temperature as a parameter, while Fig. 9b represents the dependence of intercept B as a function of inversed temperature, for the case of gate electron injection and for applied bias voltages higher than −0.4 V.

Following the same analysis, the φ_t value is calculated equal to 0.36 eV, as expected.

Due to the fact that both Ohmic and Frenkel–Poole conduction mechanisms belong to the general category of the bulk conduction mechanisms, $J(V)$ measurements should be performed in a broader voltage and temperature range ($V > 2.0$ V and $T > 393$ K) in order to get a view of the electrode limited Schottky conduction mechanism, through which the evaluation of energy barrier heights between $HfO_2|p$-Ge and $Al|HfO_2$ can be evaluated.

In order to detect the region where the conduction of the structure is governed by the Schottky mechanism, $J(V)$ measurements were performed in an applied voltage region from −5.0 to +5.0 V and temperatures higher than 430 K.

For the standard Schottky emission, expressed through

$$J = A^*T^2E^{\frac{-q(\varphi_B-\sqrt{qE/4\pi\varepsilon\varepsilon_0})}{kT}}, \quad (8)$$

where $A^* = (4\pi qm^*K^2/h^3) = 120 \times 10^4(m^*/m_0)$ A/cm^2 K^2, J is the current density, A^* is the effective Richardson constant, T is the absolute temperature, q is the electronic charge, E is the electric field, K is the Boltzmann's constant, ε_0 is the permittivity of free space, ε is the dynamic electric constant of HfO_2, $q\varphi_B$ is the Schottky barrier height, m^* is the electron effective mass in HfO_2, h is Planck's constant, and $m^*/m_0 = 0.5$ [22]. The dependence of $\ln(J/T^2)$ as a function of the square root of the electric field ($E^{1/2}$), presented in Figs. 10a and 10b, should be linear [56]. For both substrate and gate electron injection cases, the experimental data, in the temperature range from 453 to 533 K and values of electric field higher than 2.5 MV/cm (i.e., $E^{1/2} = 16 \times 10^3$ $(\text{V/m})^{1/2}$ and $V = 4.0$ V) and 2.0 MV/cm (i.e., $E^{1/2} = 14 \times 10^3$ $(\text{V/m})^{1/2}$

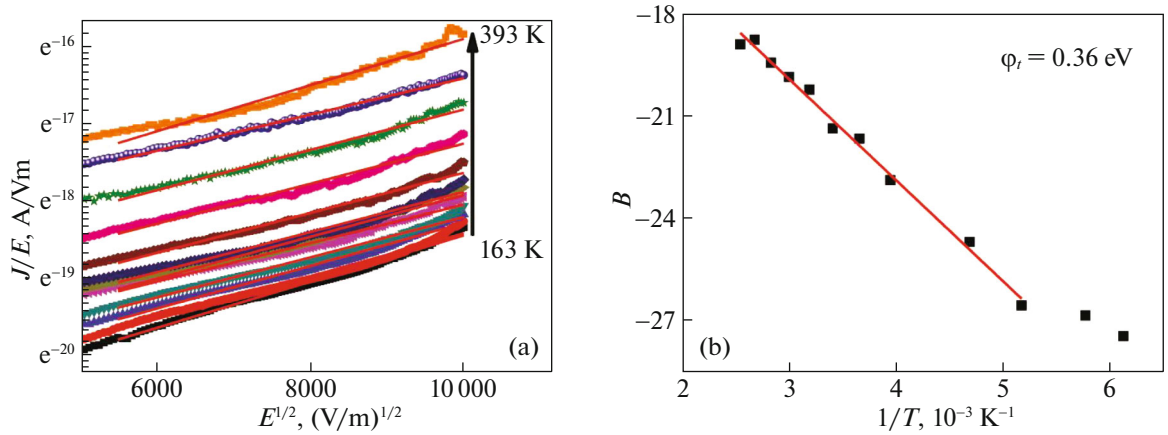

Fig. 9. (a) $\ln J/E$ vs. $E^{1/2}$ characteristics for gate electron injection for applied voltages higher than 0.4 V in the whole temperature range. (b) Intercept B as a function of $1/T$ in the same temperature range.

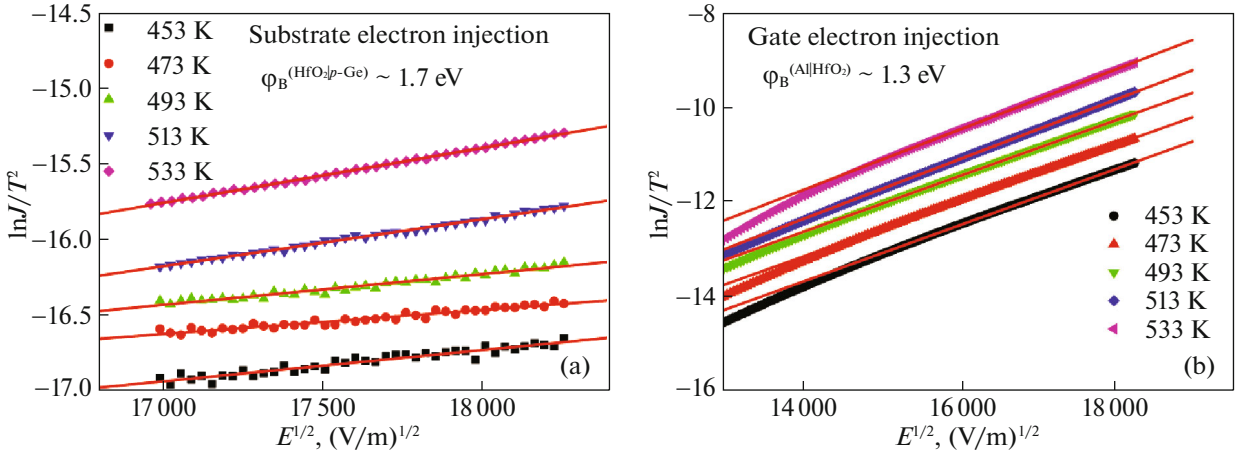

Fig. 10. $\ln J/T^2$ as a function of $E^{1/2}$ for (a) substrate and (b) gate electron injection for temperatures higher than 453 K and applied voltages higher than 4 and 3 V respectively for Al|15-nm $HfO_2|p$-Ge structures.

and $V = 3.0$ V, respectively, fit the Schottky emission theory very well (solid lines).

Through the analysis of Schottky mechanism's equation,

$$\ln\frac{J}{T^2} = \ln A^* - \frac{q\varphi_B}{kT} + \frac{\sqrt{q^3E/4\pi\varepsilon\varepsilon_0}}{kT}. \quad (9)$$

It is clear that the intercept of the fitted lines corresponds to $C = \ln A^* - q\varphi_B/kT$.

The energy barrier heights φ_B at $HfO_2|p$-Ge and Al|HfO_2 interfaces were calculated, through the intercepts of fitted lines in Figs. 10a and 10b, equal to 1.7 ± 0.2 eV and 1.3 ± 0.1 eV, respectively.

The same Schottky analysis was performed in structures exhibiting 10-nm thickness of HfO_2. Figures 11a and 11b represent the dependence of $\ln(J/T^2)$ as a function of the square root of the electric field ($E^{1/2}$) in the temperature range from 373 to 513 K and values of electric field higher than 1.0 MV/cm (i.e., $E^{1/2} = 10 \times 10^3$ (V/m)$^{1/2}$ and $V = 1.0$ V) for substrate electron injection case and from 393 to 513 K and in values of electric field higher than 2.0 MV/cm (i.e., $E^{1/2} = 14 \times 10^3$ (V/m)$^{1/2}$ and $V = 3.0$ V) for substrate electron injection case, respectively. The energy barrier heights at $HfO_2|p$-Ge and Al|HfO_2 interfaces were calculated and values of 1.7 ± 0.2 eV and 1.3 ± 0.2 eV were acquired, respectively. Thus, HfO_2 structures of 15 and 10 nm present the same results as expected.

Combining the XPS and $J(V)$ analysis results, presented above, the energy band diagram for Al|$HfO_2|p$-Ge structures is depicted in Fig. 12. Please note here that the energy band diagram represents that of an ideal MOS structure at zero bias voltage, which is a typical way to present MOS energy band diagrams [59].

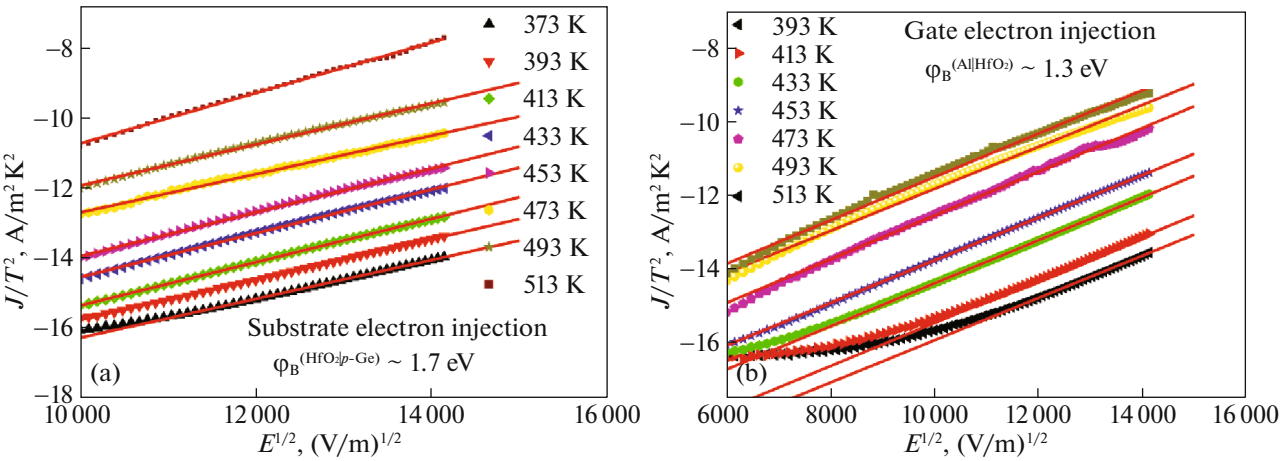

Fig. 11. $\ln J/T^2$ as a function of $E^{1/2}$ for (a) substrate and (b) gate electron injection for Al|10-nm $HfO_2|p$-Ge structures.

It is evident that the calculated, from the analysis of XPS and $J(V)$ experimental data, results of conduction and valence band offsets are in very good agreement. Specifically, taking into account the value of energy band gap of HfO_2 ($E_g = 5.3$ eV) [19, 47], the XPS evaluated conduction band offset is 1.8 ± 0.2 eV while the one extracted from $J(V)$ measurements is 1.7 ± 0.2 eV. Additionally, the XPS evaluated valence band offset is 2.8 ± 0.2 eV while the one extracted from $J(V)$ measurements is 2.9 ± 0.2 eV. Finally, the energy barrier height of Al|HfO_2, evaluated through the $J(V)$ analysis, is found equal to 1.3 ± 0.2 eV, in excellent agreement with literature values [22, 25].

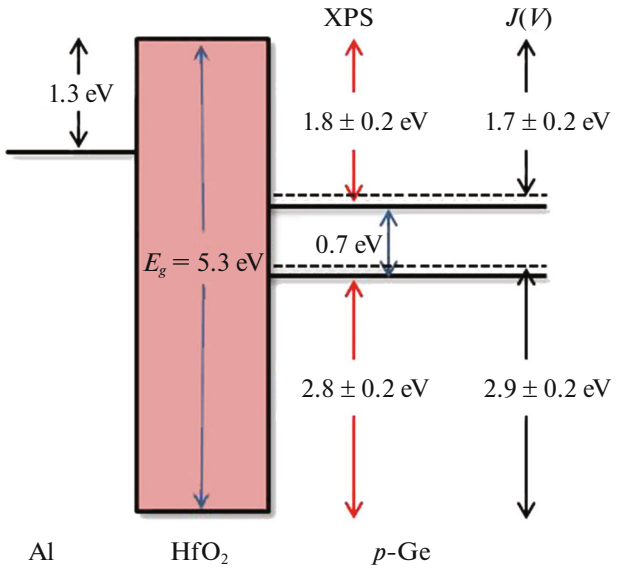

Fig. 12. Energy band diagram of Al|$HfO_2|p$-Ge structures through XPS and $J(V)$ analysis. Bold black data correspond to the XPS and $J(V)$ evaluated values, respectively, while the light ones are literature values.

CONCLUSIONS

Atomic Layer Deposited high-permittivity HfO_2 films with thicknesses varying between 3 and 15 nm were grown onto pre-cleaned p-Ge substrates and characterized structurally, chemically, and electrically through TEM, XPS and $C(V)$, $G(V)$ as well as $J(V)$ electrical measurements. XPS analysis reveals the stoichiometry of the ALD-grown HfO_2 films. Additionally, the conduction and valence band offsets of $HfO_2|p$-Ge were evaluated to be equal to 1.8 ± 0.2 eV and 2.8 ± 0.2 eV, respectively. $J(V)$ measurements, in a wide applied voltage (−5.0 to +5.0 V) and temperature (163–533 K) ranges, reveal that for both substrate and gate electron injection, the dominant conduction mechanism at voltages lower than 0.2 V ($V < 0.2$ V) is Ohmic with an activation energy 0.28 eV. At voltages higher than 0.4 V, for both substrate and gate electron injection the prevailing conduction mechanism is the Frenkel–Poole, through which the trap energy level into HfO_2 films (φ_t) is calculated to be equal to 0.36 eV. Schottky conduction mechanism is detected, as expected, in the high-voltage and high-temperature region. Specifically, for voltages higher than 3.0 V and temperatures greater than 450 K, Schottky mechanism is the prevailing one. Applying Schottky's emission model, the $HfO_2|p$-Ge as well as Al|HfO_2 energy barrier heights were evaluated equal to 1.7 ± 0.2 eV and 1.3 ± 0.2 eV, respectively. The energy band diagram of Al|$HfO_2|p$-Ge structures is constructed, combining the experimental results of both XPS and $J(V)$ measurements. The calculated values of conduction and valence band offsets via XPS and $J(V)$ measurements are in very good agreement.

ACKNOWLEDGMENTS

This research has been co-financed by the Operational Program "Human Resources Development, Education,

and Lifelong Learning" and is co-financed by the European Union (European Social Fund) and Greek national funds.

The authors are grateful to Dr. A. Travlos from the Institute of Nanoscience and Nanotechnology, NCSR "Demokritos" for the TEM analysis.

CONFLICT OF INTEREST

The authors declare that they have no conflict of interest.

REFERENCES

1. P. Svarnas, M. A. Botzakaki, G. Skoulatakis, S. Kennou, S. Ladas, C. Tsamis, S. N. Georga, and Ch. A. Krontiras, Thin Solid Films **599**, 49 (2016).
2. Q. Xie, S. Deng, M. Schaekers, D. Lin, M. Caymax, A. Delabie, X.-P. Qu, Y.-L. Jiang, D. Deduytsche, and C. Detavernier, Semicond. Sci. Technol. **27**, 074012 (2012).
3. S. Tagaki, N. Taoka, and M. Takenaka, ECS Trans. **19**, 67 (2009).
4. M. Takenaka, R. Zhang, and S. Takagi, Jpn. J. Appl. Phys. **54**, 04DA02 (2015).
5. S. Takagi, T. Maeda, N. Taoka, M. Nishizawa, Y. Morita, K. Ikeda, Y. Yamashita, M. Nishikawa, H. Kumagai, R. Nakane, S. Sugahara, and N. Sugiyama, Microelectron. Eng. **84**, 2314 (2007).
6. A. Toriumi, T. Tabata, C. H. Lee, T. Nishimura, K. Kita, and K. Nagashio, Microelectron. Eng. **86**, 1571 (2009).
7. M. A. Botzakaki, A. P. Kerasidou, L. Sygellou, V. Ioannou-Sougleridis, N. Xanthopoulos, S. Kennou, S. Ladas, N. Z. Vouroutzis, Th. Speliotis, and D. Skarlatos, ECS Solid State Lett. **1**, 32 (2012).
8. M. A. Botzakaki, A. P. Kerasidou, N. Xanthopoulos, D. Skarlatos, S. Kennou, S. Ladas, S. N. Georga, and C. A. Krontiras, Phys. Status Solidi C **10**, 137 (2012).
9. A. P. Kerasidou, M. A. Botzakaki, N. Xanthopoulos, S. Kennou, S. Ladas, S. N. Georga, and C. A. Krontiras, J. Vac. Sci. Technol. A **31**, 01A1261 (2013).
10. M. A. Botzakaki, G. Skoulatakis, N. Xanthopoulos, V. Gianneta, A. Travlos, S. Kennou, S. Ladas, C. Tsamis, E. Makarona, S. N. Georga, and C. A. Krontiras, J. Vac. Sci. Technol. A **36**, 01A120 (2018).
11. M. A. Botzakaki, N. Xanthopoulos, E. Makarona, C. Tsamis, S. Kennou, S. Ladas, S. N. Georga, and C. A. Krontiras, Microelectron. Eng. **112**, 208 (2013).
12. M. A. Botzakaki, PhD Thesis (Univ. of Patras, Patras, Greece, 2015).
13. S. Fadida, F. Palumbo, L. Nyns, D. Lin, S. van Elshocht, M. Caymax, and M. Eizenberg, J. Vac. Sci. Technol. B **32**, 03D105 (2014).
14. R. Zhang, P.-C. Huang, L. Ju-Chin, N. Taoka, M. Takenaka, and S. Takagi, IEEE Trans. Electron. Dev. **60**, 927 (2013).
15. D. Tahir, E. K. Lee, S. K. Oh, T. T. Tham, H. J. Kang, J. Jin, S. Heo, J.-C. Park, J. G. Chung, and J. C. Lee, Appl. Phys. Lett. **94**, 212902 (2009).
16. S. Heo, D. Tahir, J. G. Chung, J. Ch. Lee, K. Kim, J. Lee, H.-I. Lee, G. S. Park, S. K. Oh, H. J. Kang, P. Choi, and B.-D. Choi, Appl. Phys. Lett. **107**, 182101 (2015).
17. G. D. Wilk, R. M. Wallace, and J. M. Anthony, J. Appl. Phys. **89**, 5243 (2001).
18. F.-C. Chiu, J. Appl. Phys. **100**, 114102 (2006).
19. E. Bersch, S. Rangan, and R. A. Bartynski, Phys. Rev. B **78**, 085114 (2008).
20. K. J. Hubbard and D. G. Schlom, J. Mater. Res. **11**, 2757 (1996).
21. L. Kang, B. H. Lee, W. J. Qi, Y. Jeon, R. Nieh, S. Gopalan, K. Onishi, and J. C. Lee, IEEE Electron. Dev. Lett. **21**, 181 (2000).
22. H. W. Chen, F. C. Chiu, C. H. Liu, S. Y. Chen, H. S. Huang, P. C. Juan, and H. L. Hwang, Appl. Surf. Sci. **254**, 6112 (2008).
23. P. M. Tirmali, A. G. Khairnar, B. N. Joshi, and A. M. Mahajan, Solid-State Electron. **62**, 44 (2011).
24. F.-C. Chiu, S.-A. Lin, and J. Y. Lee, Microelectron. Reliab. **45**, 961 (2005).
25. W. J. Zhu, T.-P. Ma, T. Tamagawa, J. Kim, and Y. Di, IEEE Electron. Dev. Lett. **23**, 97 (2002).
26. P. W. Peacock and J. Robertson, J. Appl. Phys. **92**, 4712 (2002).
27. H. Na, J. Lee, J. Jeong, T. Kim, and H. Sohn, Appl. Phys. A **124**, 259 (2018).
28. M. A. Botzakaki, G. Skoulatakis, S. Kennou, S. Ladas, C. Tsamis, S. N. Georga, and C. A. Krontiras, J. Phys. D: Appl. Phys. **49**, 3851041 (2016).
29. I.-S. Park, Y. C. Jung, S. Seong, J. Ahn, and S. Bo Lee, J. Vac. Sci. Technol. A **33**, 01A153 (2015).
30. L. Zhao, H. Liu, X. Wang, Y. Wang, and Sh. Wang, Nanomaterials **9**, 697 (2019).
31. G. Mavrou, S. Galata, P. Tsipas, A. Sotiropoulos, Y. Panayiotatos, and A. Dimoulas, J. Appl. Phys. **103**, 014506 (2008).
32. H.-S. Jung, I-H. Yu, H. K. Kim, S. Y. Lee, J. Lee, Y. Choi, Y. J. Chung, N.-I. Lee, T. J. Park, J.-H. Choi, and C. S. Hwang, IEEE Trans. Electron. Dev. **59**, 9 (2012).
33. M. Caymax, S. van Elshocht, M. Houssa, A. Delabie, T. Conard, M. Meuris, M. M. Heyns, A. Dimoulas, S. Spiga, M. Fanciulli, J. W. Seo, and L. V. Goncharova, Mater. Sci. Eng. B **135**, 256 (2006).
34. Y.-Q. Cao, B. Wu, D. Wu, and A.-D. Li, Nanoscale Res. Lett. **12**, 370 (2017).
35. In-S. Park, Y. C. Jung, S. Seong, J. Ahn, and S. Bo Lee, J. Vac. Sci. Technol. A **33**, 01A153 (2015).
36. G. He, J. Zhang, Z. Sun, J. Lv, H. Chen, and M. Liu, AIP Adv. **6**, 025003 (2016).
37. Q. Xie, D. Deduytsche, M. Schaekers, M. Caymax, A. Delabie, X.-P. Quc, and C. Detavernier, Electrochem. Solid State **14** (5), G20 (2011).
38. D. H. Lee, H. Lee, H. Imajo, Y. Yoshioka, and T. Kanashima, J. Korean Phys. Soc. **59**, 2503 (2011).
39. K. Li, Sh. Li, N. Li, D. A. Dixon, and T. M. Klein, J. Phys. Chem. C **114**, 14061 (2010).
40. D. M. Hausmann and R. G. Gordon, J. Cryst. Growth **249**, 251 (2003).

41. S. Gieraltowska, L. Wachnicki, B. S. Witkowski, R. Mroczynski, P. Dluzewski, and M. Godlewski, Thin Solid Films **577**, 97 (2015).
42. M.-H. Cho, Y. S. Roh, C. N. Whang, K. Jeong, S. W. Nahm, D.-H. Ko, J. H. Lee, N. I. Lee, and K. Fujihara, Appl. Phys. Lett. **81**, 472 (2002).
43. C.-C. Cheng, C.-H. Chien, G.-L. Luo, C.-H. Yang, M.-L. Kuo, J.-H. Lin, C.-K. Tseng, and C.-Y. Chang, J. Electrochem. Soc. **154**, G155 (2007).
44. S. Ladas, L. Sygellou, S. Kennou, M. Wolf, G. Roeder, A. Nutsch, M. Rambach, and W. Lerch, Thin Solid Films **520**, 871 (2011).
45. E. A. Kraut, R. W. Grant, J. R. Waldrop, and S. P. Kowalczyk, Phys. Rev. B **28**, 1965 (1983).
46. M. C. Cheynet, S. Pokrant, F. D. Tichelaar, and J.-L. Rouvière, J. Appl. Phys. **101**, 054101 (2007).
47. E. S. M. Goh, T. P. Chen, C. Q. Sun, and Y. C. Liu, J. Appl. Phys. **107**, 024305 (2010).
48. E. P. Gusev, H. Shang, M. Copel, M. Gribelyuk, C. D'Emic, P. Kozlowski, and T. Zabel, Appl. Phys. Lett. **85**, 2334 (2004).
49. M. M. Frank, H. Shang, S. Rivillon, F. Amy, C.-L. Hsueh, V. K. Paruchuri, R. T. Mo, M. Copel, E. P. Gusev, M. A. Gribelyuk, and Y. J. Chabal, Solid State Phenom. **103–104**, 3 (2005).
50. A. Delabie, R. L. Puurunen, B. Brijs, M. Caymax, T. Conard, B. Onsia, O. Richard, W. Vandervorst, C. Zhao, M. M. Viitanen, H. H. Brongersma, M. de Ridder, L. V. Goncharova, E. Garfunkel, T. Gustafsson, W. Tsai, M. M. Heyns, and M. Meuris, J. Appl. Phys. **97**, 064104 (2005).
51. M. M. Frank, S. J. Koester, M. Copel, J. A. Ott, V. K. Paruchuri, and H. Shang, Appl. Phys. Lett. **89**, 112905 (2006).
52. K. Martens, O. C. Chui, G. Brammertz, B. de Jaeger, D. Kuzum, M. Meuris, M. M. Heyns, T. Krishnamohan, K. Saraswat, H. E. Maes, and G. Groeseneken, IEEE Trans. Electron. Dev. **55**, 547 (2008).
53. K. S. Agrawal, V. S. Patil, A. G. Khairnar, and A. M. Mahajan, Appl. Surf. Sci. **364**, 747 (2016).
54. E. H. Nicollian and J. R. Brews, *MOS (Metal Oxide Semiconductor) Physics and Technology* (Wiley—Interscience, New York, NY, 1982).
55. W. A. Hill and C. C. Coleman, Solid State Electron. **23**, 987 (1973).
56. S. M. Sze, *Physics of Semiconductor Devices* (Wiley, New York, 1981), p. 402.
57. M.-T. Wang, Sh.-Y. Deng, T.-H. Wang, Bonds Yi-Yi Cheng, and J. Y.-M. Lee, J. Electrochem. Soc. **152**, G542 (2005).
58. F.-C. Chiu, Z.-H. Lin, C.-W. Chang, Ch.-Ch. Wang, K.-F. Chuang, Ch.-Y. Huang, J. Y.-M. Lee, and H.-L. Hwang, J. Appl. Phys. **97**, 034506 (2005).
59. T. Tan, Z. Liu, H. Lu, W. Liu, F. Yan, and W. Zhang, Appl. Phys. A **97**, 475 (2009).